Sensitivity of the Lorenz energy cycle of the global ocean

John Ssebandeke[1] · Jin-Song von Storch[1] · Nils Brüggemann[1,2]

Abstract

We re-examine the Lorenz energy cycle (LEC) for the global ocean by assessing its sensitivity to model and forcing differences. We do so by comparing LECs derived from two simulations based on different eddy-rich ocean models, ICON-O and MPI-OM, both driven by NCEP/NCAR reanalysis, and by comparing LECs derived from two simulations generated using ICON-O model but driven by two different reanalyses, NCEP/NCAR and ERA5. Regarding model difference, we find weaker eddy kinetic energy, k_e, in the ICON-O simulation than in the MPI-OM simulation. We attribute this to the higher horizontal resolution of MPI-OM in the Southern Ocean. The weaker k_e in ICON-O is not caused by the lack of eddy available potential energy, p_e, but by the strong dissipation of p_e and the resulting weak conversion from p_e to k_e. Regarding forcing difference, we find that considerably more mechanical energy is generated by the ERA5 forcing, which has a higher spatial-temporal resolution compared to the NCEP/NCAR forcing. In particular, the generation of k_e, which also contains the resolved part of the internal wave spectrum, is enhanced by about 1 TW (40%). However, the dominance of the baroclinic and the barotropic pathways forces the enhanced generation of k_e to be balanced by an enhanced dissipation in the surface layer. The gross features of LEC are insensitive to both model and forcing differences, picturing the ocean as an inefficient "windmill" that converts only a small portion of the inputted mechanical energy into the interior mean and transient circulations.

Keywords Lorenz energy cycle (LEC) · ERA5 · NCEP/NCAR · ICON-O · MPI-OM

1 Introduction

The oceanic and atmospheric general circulation comprises both the time-mean large-scale circulation and the transients, which are dominated by synoptic variations in the atmosphere and mesoscale eddies in the ocean. These components of general circulation exchange energy, and this energy-exchange is well quantified by the Lorenz energy cycle (LEC) ((Lorenz, 1955) and references therein). The LEC is a quantitative framework for identifying how energy in the ocean and atmosphere proceeds, through transformation, from its generation to its dissipation, and it has become a standard tool for studying the energetics of the general circulation. While a robust picture of the atmospheric LEC has been established, through evaluations based on data of different qualities including those from various reanalyses (Lorenz, 1967; Oort, 1964; Li et al., 2007; Kim and Kim, 2013; Marques et al., 2009), the picture of the oceanic LEC is much less established. The situation comes about, since the oceanic mesoscale eddies, whose spatial scale is of $O(100\,\text{km})$ and hence one order of magnitude smaller than that of synoptic variations—$O(1000\,\text{km})$—cannot be observed at a high enough frequency with a sufficient spatial coverage, nor truly be captured by the current ocean reanalyses. Capturing these eddies is however important for properly assessing energy transfer between the mean and the transient compartments of circulation. One way to advance is to use simulations in which mesoscale eddies are largely resolved. To our knowledge, there exist one estimate for the LEC of the global ocean (von Storch et al., 2012). It is not clear whether the basic characteristics of the previously estimated LEC are model independent, and therefore, the extent to which the previous estimates can reliably reflect the energy transfer processes related to the LEC in the real ocean is unclear. It is also not clear whether and to what extent the previously identified energy transfer processes change when an ocean model

✉ John Ssebandeke
  john.ssebandeke@mpimet.mpg.de

1 Max-Planck-Institute for Meteorology, Hamburg, Germany

2 Institute of Oceanography, University of Hamburg, Hamburg, Germany

is forced with surface fluxes derived from a more advanced atmospheric reanalysis. This paper addresses these two questions.

We do so by comparing estimates of the ocean LEC obtained from two pairs of simulations. The first pair is performed with the same ocean model forced with surface fluxes derived from two different reanalyses—the NCEP/NCAR (hereafter NCEP) (Kalnay et al., 1996) and the newly released ERA5 reanalysis (hereafter ERA5) (Hersbach et al., 2020). We will refer to differences between this pair of simulations as "forcing differences" (note that other forcing products leading to potentially different LECs are not included within our reference). The second pair consists of simulations performed with two different ocean models— MPI-OM (Marsland et al., 2003; Jungclaus et al., 2013) and ICON-O (Korn, 2017; Korn et al., 2022)—but forced with the surface fluxes derived from the same reanalysis. Differences between this other pair of simulations will be referred to as "model differences" (note again that we only refer to the differences between these two models). The MPI-OM simulation is the one from which the previous estimate by von Storch et al. (2012) is derived and the ICON-O simulation is the same as used for the aforementioned inter-comparison with respect to different forcing products. ICON-O is a newly developed model at the Max Planck Institute for Meteorology (Korn et al., 2022).

The comparison will be based on the balance equations for the mean and the transient kinetic energy, K_m and K_e, and those for the mean and transient available potential energy, P_m and P_e. While the definitions of K_m and K_e are straightforward, those of P_m and P_e rely on approximations. In this paper, we follow the definition originally proposed by Lorenz (1955) and approximate the available potential energy in terms of the deviations of density from a spatially constant reference density ρ_{ref} (Oort et al., 1994). Potential energy associated with these density deviations can be, at least in principle, turned into motions via the related pressure gradients. The resulting LEC, including the definitions of all terms, is introduced in more detail in the Appendix. We note that this definition of available potential energy, together with its associated energy transfers and budgets, differs from the other considerations, e.g., that by Winters et al. (1995). As reviewed by von Storch (2019), the LEC as defined, e.g., by Oort et al. (1994); von Storch et al. (2012) focuses on the energy transfers associated with the mesoscale eddy field, while the one defined in Winters et al. (1995) focuses on the effect of mixing related to diabatic processes inside the ocean.

This paper is organized as follows: Sect. 2 describes the models and the surface forcing. Section 3 describes the LEC estimated from the ICON-O simulation forced with the NCEP forcing. Differences arising from using different models and from using different surface forcings will be addressed in Sect. 4 Discussions and a summary are provided in the final section.

2 The numerical simulations

2.1 Numerical models

ICON-O (Korn, 2017; Korn et al., 2022) and MPI-OM (Marsland et al., 2003; Jungclaus et al., 2013) are both primitive equation models; however, they employ completely different model architectures and are coupled to completely different sea ice models. ICON-O was designed to improve parallel computing on high performance computers and has recently become the work horse at Max-Planck Institute for Meteorology. The Gent–McWilliams parameterization (Gent and Mcwilliams, 1990) that describes the effect of mesoscale eddies is switched off in MPI-OM and in all ICON-O configurations considered in this study. Vertical mixing is parameterized using the Richardson-number dependent formulation following Pacanowski and Philander (1981) in MPI-OM and by the TKE scheme following Gaspar et al. (1990) in ICON-O. These parameterizations are responsible for most of the diapycnal mixing in the upper ocean.

In the vertical, both ICON-O and MPI-OM use the standard z-coordinate framework. In the horizontal, both are considered to have a nominal resolution of about 10 km, which allows resolving the bulk of mesoscale eddies outside the polar regions. However, MPI-OM is formulated on a tripolar grid with rectangular-shaped grid cells, whereas ICON-O is formulated on an icosahedral grid with triangular-shaped grid cells. The different structure of the grids results in a different number and a different distribution of grid points. The ICON-O grid has a total of 3,699,276 wet grid points in the surface layer and total 128 vertical levels. The MPIOM grid has a total of 5,558,745 wet grid points in the surface layer and total 80 vertical levels. The larger number of grid points in MPI-OM is due to the fact that the grid size, south of the equator, is refined based on the cosine of the latitude— $0.1° \cos(\phi)$, where ϕ is the latitude. Thus, the MPIOM grid in the southern hemisphere is much less uniform, ranging from about 10 km near the equator, up to 5–6 km near 60°S, and up to about 2–3 km in the Weddell and Ross sea. In the northern hemisphere, the grid size of the MPI-OM grid is more comparable to that of ICON-O.

Overall, there are considerable differences between ICON-O and MPI-OM in the numerics, in the applied parameterizations, and horizontal and vertical grid used. This is why we consider both model configurations as independent. A comparison of the LEC diagnosed for both of these model configurations in Sect. 3 allows us to identify the robust and model-independent features of the ocean's energy pathways.

To enhance comparability, the treatment of the output for both ICON-O simulations are carried out in the same way as it was done with the MPI-OM simulation in von Storch et al. (2012). The MPI-OM simulation was obtained by forcing MPI-OM with the NCEP reanalysis, hereafter referred to as MPIOM/NCEP (see von Storch et al. (2012) for more details of the setup). One of the two ICON-O simulations, hereafter referred to as ICON/NCEP, is conducted exactly in the same way as MPIOM/NCEP. It is spun up for 25 years using heat, freshwater, and momentum fluxes obtained from the German Ocean Model Inter-comparison Project (OMIP) climatology forcing (Röske, 2006). After the spin-up phase, the forcing is switched to the 6-hourly NCEP reanalysis dataset (Kalnay et al., 1996) and the model is integrated from 1948 to 2019. The second ICON-O simulation, ICON/ERA5, is generated by branching from the ICON/NCEP simulation in 1980 and replacing the NCEP forcing with the ERA5 forcing dataset (Hersbach et al., 2020). A summary of the model simulations is presented in Table 1.

Data output from the same 10 years, namely, from 2001 to 2010, is used to estimate the 10-year averaged LEC in the three simulations. Analogous to von Storch et al. (2012), eddies are defined as deviations from the time mean that fluctuate on timescales ranging from the model time step to 10 years. The individual terms of the LEC, namely, the energy reservoirs K_m, K_e, P_m, and P_e, the generations of these reservoirs $G(K_m)$, $G(P_e)$, $G(K_m)$, and $G(K_e)$, as well as the conversion terms $C(P_m, K_m)$, $C(P_m, P_e)$, $C(P_e, K_e)$, and $C(K_m, K_e)$, are defined in the Appendix. For a conversion term $C(X, Y)$, the convention is such that $C(X, Y) = -C(Y, X)$ and the direction of $C(X, Y)$ goes from X to Y. Hereafter, we use capital letters to indicate globally integrated energy terms and small letters to indicate local energy terms. Since the magnitudes of the mean and eddy available potential energy depend on the reference density ρ_{ref} used, it is difficult to discuss the magnitudes of these energy terms.

There might also be an error in P_m obtained from MPIOM/NCEP, which is two orders of magnitudes larger than P_m in ICON/NCEP and ICON/ERA5. This however cannot be further confirmed, since not all data from MPIOM/NCEP, which was carried out more than 10 years ago, are available for us. P_m and P_e will nevertheless be calculated and listed for the sake of completeness. The data still available from MPIOM/NCEP are the 3-dimensional velocities and the global integrated numbers as listed in von Storch et al. (2012). The comparison with the MPIOM/NCEP LEC, to be discussed in Sect. 4.1, will hence be based essentially on the published results (von Storch et al., 2012). Analogous to MPIOM/NCEP, the second moments needed for calculating the LEC terms for ICON/NCEP and ICON/ERA5 are generated at every model time step and outputted on a monthly basis. We note that in this way, p_e and k_e result from transient motions that vary on timescales ranging from the model time step to the time average period of 10 years. We expect that the transients are dominated by mesoscale eddies arising from baroclinic and barotropic instability throughout the ocean and by near-inertial waves near the surface. For simplicity, we refer to k_e and p_e as eddy kinetic energy and eddy available potential energy, even though they are not related to mesoscale eddies only.

2.2 Surface forcing

We use two reanalyses data sets ERA5 (Hersbach et al., 2020) and NCEP (Kalnay et al., 1996) as surface forcing for the temperature, salinity, and momentum equations of the ICON-O simulations. The wind stress, used to mechanically drive ICON-O and MPI-OM, is thereby taken directly from the reanalyses products without considering the ocean velocity in the derivation of the stresses. This leads to an overestimation of the wind energy input, which needs to be kept in mind when interpreting our results (Zhai et al., 2012). The heat and freshwater flux are derived based on bulk formulae using a combination of meteorological variables from the reanalyses and the simulated ocean surface temperature.

Table 1 Summary of the simulations

Model	ICON/NCEP ICON-O	ICON/ERA5 ICON-O	MPIOM/NCEP MPI-OM
Model horizontal resolution	10 km	10 km	10 km. South of the equator the grid size is $0.1° \cos(\phi)$ where ϕ is latitude
Model vertical resolution	128 (8–200) m	128 (8–200) m	80 (10–279) m
Forcing	NCEP/NCAR	ERA5	NCEP/NCAR
Forcing resolution	200 km, 6 h	31 km, 1 h	200 km, 6 h

The surface forcing from the NCEP reanalysis product differs significantly from the ERA5 reanalysis product, concerning both the mean and the variability of the surface fluxes. The higher spatial-temporal resolution of ERA5 (31 km, hourly) relative to NCEP (200 km, 6 hourly) leads to stronger variability in the surface fluxes in ERA5 than in NCEP. As shown by the difference between standard deviation of ERA5 fluxes and that of NCEP fluxes (Fig. 1), enhanced variability is found for all three fluxes in most part of the ocean outside the polar regions. Regarding the wind stress, the largest difference in variability is found in the storm track regions over the mid-latitude oceans where a maximum of about $0.02\ N/m^2$ is reached. A similar picture is found for the heat flux, where the difference in the variability reaches values up to $30\ W/m^2$ in the Gulf Stream and Kuroshio. For the freshwater flux, the largest difference of more than $4\ mm/day$

Fig. 1 Difference in the standard deviation of surface forcing (ERA5 minus NCEP) for **a** magnitude of wind stress, **b** net heat flux, and **c** net fresh water flux, obtained from 1 hourly ERA5 reanalysis and 6 hourly NCEP reanalysis over the common 10-year period from 2001 to 2010. The standard deviations of heat and freshwater are estimated using monthly averages and therefore represent time-variations between 1 month and 10 years
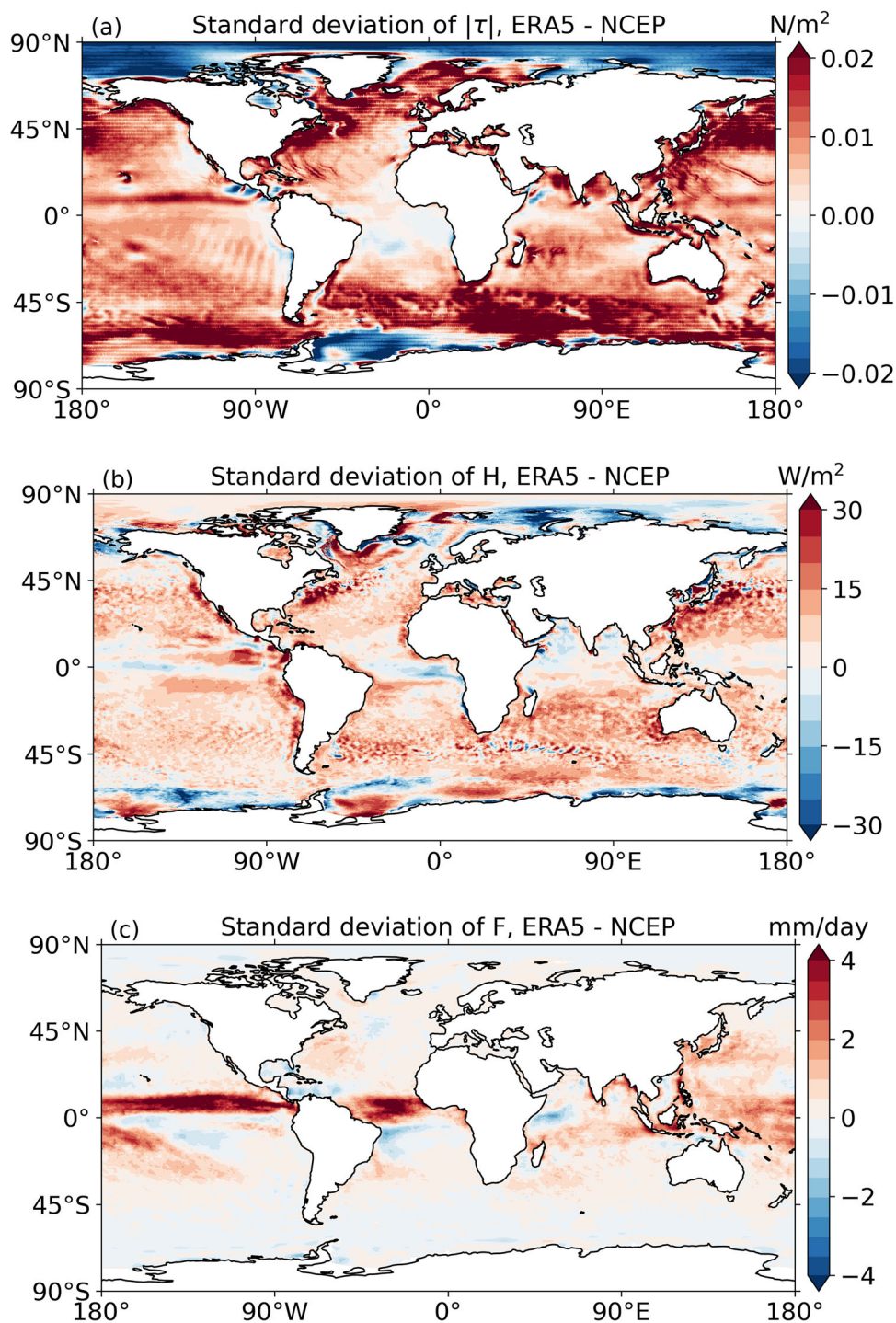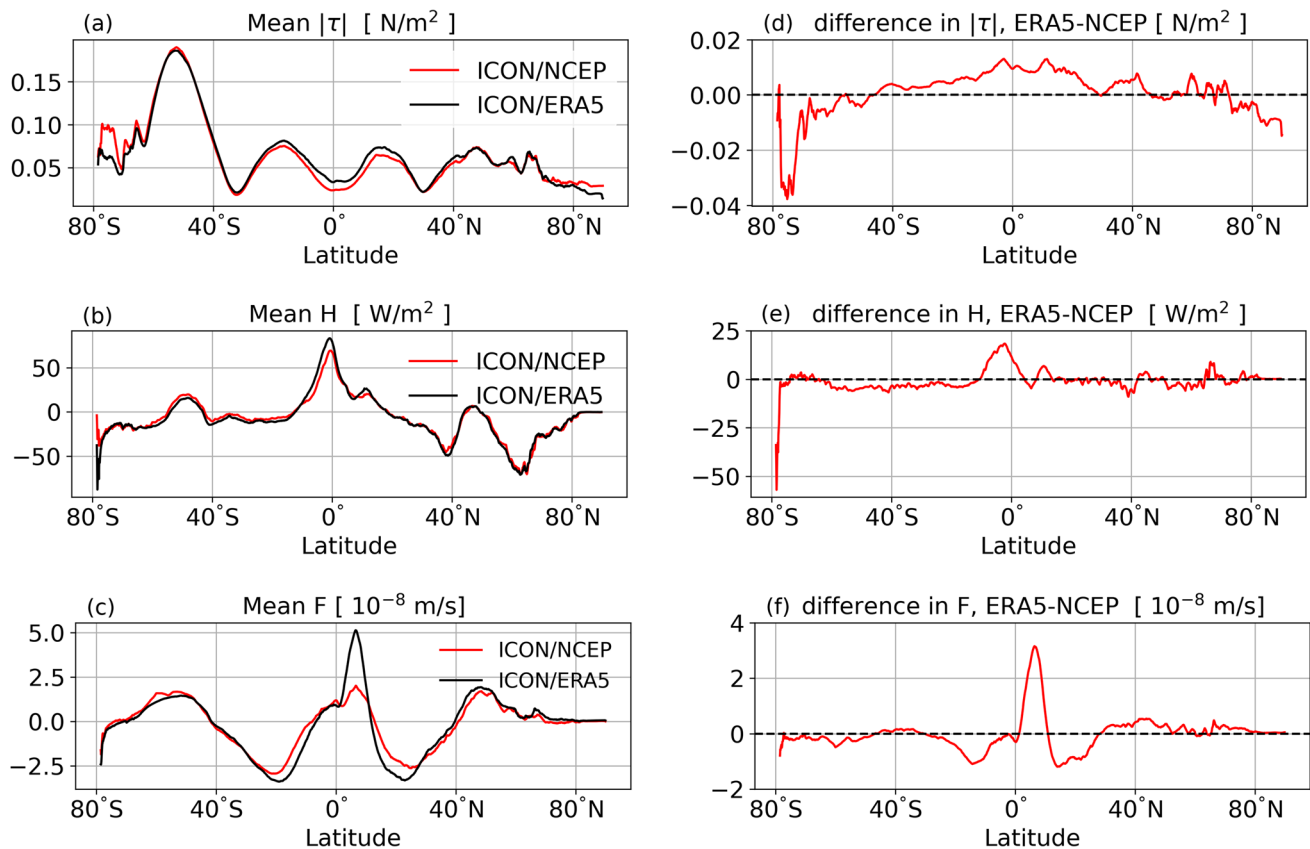
Fig. 2 Time-mean zonal-mean fluxes (left) of momentum (top), heat (middle), and fresh water (bottom), derived from ERA5 (black) and NCEP (red) reanalyses and the difference between ERA5 and NCEP (right). The fluxes are calculated for the common 10-year period from 2001 to 2010

is found in the tropics, especially in the central and eastern tropical Pacific and in the tropical Atlantic. These differences in standard deviations are of comparable magnitudes as the zonally averaged time-mean fluxes shown Fig. 2.

The zonally averaged time-mean fluxes obtained from the ERA5 reanalysis (black lines in the left column of Fig. 2) are mostly comparable to those obtained from the NCEP reanalysis (red lines in the left column of Fig. 2). However, there exist also noticeable differences between the two (right column of Fig. 2). Relative to NCEP, ERA5 wind stress is stronger over the tropical and subtropical oceans and weaker over the high-latitude oceans. ERA5 heat flux is noticeably larger than the NCEP heat flux near and south of the equator. For the freshwater flux, the ERA5 flux in a narrow latitudinal band just north of the equator is more than twice as strong as the NCEP flux.

The large differences in the variability of fluxes, together with the changes in the mean fluxes, could produce differences in the generation of kinetic energy and available potential energy at the sea surface. Whether and how these different generations affect the energy pathways inside the ocean will be analyzed in Sect. 4.2.

3 Lorenz energy cycle in ICON/NCEP

This section describes the LEC derived from ICON/NCEP, which will be used as the reference LEC for assessing the sensitivity of LEC to model difference and to forcing difference. The ICON/NCEP LEC is depicted by black bold numbers in Fig. 3. Overall, the generation and dissipation terms, G_X and D_X, are larger than the conversion terms, $C(X, Y)$. This suggests that a large portion of the energy input does not lead to transformations between eddies and mean circulation or between kinetic and potential energy but that the energy which is put in at the ocean surface might be dissipated without being transformed to another energy compartment of the LEC. The generation of P_e, $G(P_e)$ in ICON/NCEP is consistent with the new findings in Bishop et al. (2020), namely, that when $G(P_e)$ is decomposed into two parts, one associated to the seasonal cycle and the other with all non-seasonal time scales, the latter is a sink for P_e, especially along the Gulf stream, Kuroshio, and in the tropical oceans. The strongest conversion among the LEC energy compartments is that between mean available potential and eddy available potential energy $C(P_m, P_e)$ and the

Fig. 3 LEC for ICON/NCEP (black), ICON/ERA5 (blue), and MPIOM/NCEP (red). The values corresponding to MPIOM/NCEP are adopted from von Storch et al. (2012). The energy reservoirs are in exajoules (EJ, 10^{18}) and zettajoules (ZJ, 10^{21}). The generation, exchange, and dissipation terms are in terawatts (TW, 10^{12}). The red bracketed numbers are model differences (MPIOM/NCEP minus ICON/NCEP) and the blue bracketed numbers are forcing differences (ICON/ERA5 minus ICON/NCEP). Only those differences, which are larger than the typical magnitude of sampling errors, are indicated by bracketed numbers

$D(P_m)$
1.66 (0.25)
1.62 (0.21)
1.41 ± 0.01 TW

$D(K_m)$
1.10 ± 0.06 TW
1.28 (0.18)
1.36 (0.26)

$G(P_m)$
1.84 ± 0.00 TW
2.12 (0.28)
2.00 (0.16)

P_m
1.52 ± 0.01 ZJ
1.55 (0.03)
166

$C(P_m, K_m)$
0.49 (0.09)
0.40
0.40 ± 0.04 TW

K_m
0.86 ± 0.02 EJ
0.95 (0.09)
1.27 (0.41)

$G(K_m)$
1.67 ± 0.10 TW
1.89 (0.22)
1.85 (0.18)

$C(P_m, P_e)$
0.83 (0.07)
0.91 (0.07)
0.84 ± 0.03 TW

ICON/NCEP
ICON/ERA5
MPIOM/NCEP

$C(K_m, K_e)$
0.17 ± 0.00 TW
0.21 (0.04)
0.11 (-0.06)

$G(P_e)$
0.84 ± 0.01 TW
1.03 (0.19)
0.58 (-0.26)

P_e
9.20 ± 0.17 EJ
10.39 (1.19)
6.38 (-2.82)

$C(P_e, K_e)$
0.49 ± 0.00 TW
0.52 (0.03)
0.73 (0.24)

K_e
2.90 ± 0.09 EJ
3.45 (0.55)
3.55 (0.65)

$G(K_e)$
2.26 ± 0.10 TW
3.22 (0.96)
2.19

$D(P_e)$
1.19 ± 0.02 TW
1.41 (0.22)
0.68 (-0.51)

$D(K_e)$
2.91 ± 0.10 TW
3.95 (1.04)
3.03 (0.12)

consecutive conversion from eddy available into eddy kinetic energy $C(P_e, K_e)$. This energy pathway is frequently associated with baroclinic instability arising from vertical shear of horizontal velocity.

Hereafter, we will refer to the conversion from P_m via P_e to K_e as the baroclinic pathway. However, it should be noted that also a considerable amount of eddy available potential energy is introduced and an even larger amount is dissipated along this pathway. We would like to note that diapycnal mixing within the geostrophic mesoscale circulation is expected to be small in reality. In this regard, the large dissipation of P_e might either occur within regions of enhanced diapycnal mixing like the upper-ocean mixed layer or it occurs due to numerical mixing by the discretized tracer advection. In the ICON/NCEP run, the baroclinic pathway consists of $C(P_m, P_e)$ that amounts to 0.84 TW and $C(P_e, K_e)$ that amounts to 0.49 TW.

The third strongest conversion is that of $C(K_m, P_m)$, which amounts to about 0.4 TW. The weakest conversion is $C(K_m, K_e)$, which amounts to about 0.17 TW. Since $C(K_m, K_e)$ is related to momentum flux along the horizontal gradient of horizontal velocity, and since a strong horizontal shear in horizontal velocity can result in barotropic instability, $C(K_m, K_e)$ will be hereafter referred to as the barotropic

pathway. Below, we describe the conversions associated with different pathways in ICON/NCEP in more detail.

Integrated vertically, the conversion from p_m to p_e (Fig. 4, top) tends to occur at the same place where p_e is converted into k_e (Fig. 4, bottom), such as along the Gulf Stream and Kuroshio, around Azores in the North Atlantic, along fronts in the Southern Ocean, as well as in the central eastern equatorial Pacific and the central eastern equatorial Atlantic. Outside the equatorial region, this co-occurrence is indicative of the baroclinic pathway from p_m to p_e and eventually to k_e. Less clear is the co-occurrence near the equator where geostrophy breaks down, but the energy is nevertheless transferred from p_m to p_e and subsequently to k_e as if it is driven by baroclinic instability. In the Gulf Stream and Kuroshio, especially where the two currents start to be detached from the coast, and also occasionally in Southern Ocean fronts, the opposite pathway going from k_e to p_e and eventually to p_m is also observed.

Figure 5 shows the latitude and depth cross-section of the zonally integrated conversion $c(p_m, p_e)$ and the conversion $c(p_e, k_e)$. Since these conversions occur mainly along the boundary currents outside the Southern Ocean, but all over the place in the Southern Ocean, the zonally integrated conversions are much stronger in the Southern Ocean than

Fig. 4 Horizontal distribution of the vertically integrated conversion rate from mean available potential energy to eddy available potential energy, $c(p_m, p_e)$ (top), and from eddy available potential energy to eddy kinetic energy, $c(p_e, k_e)$ (bottom)
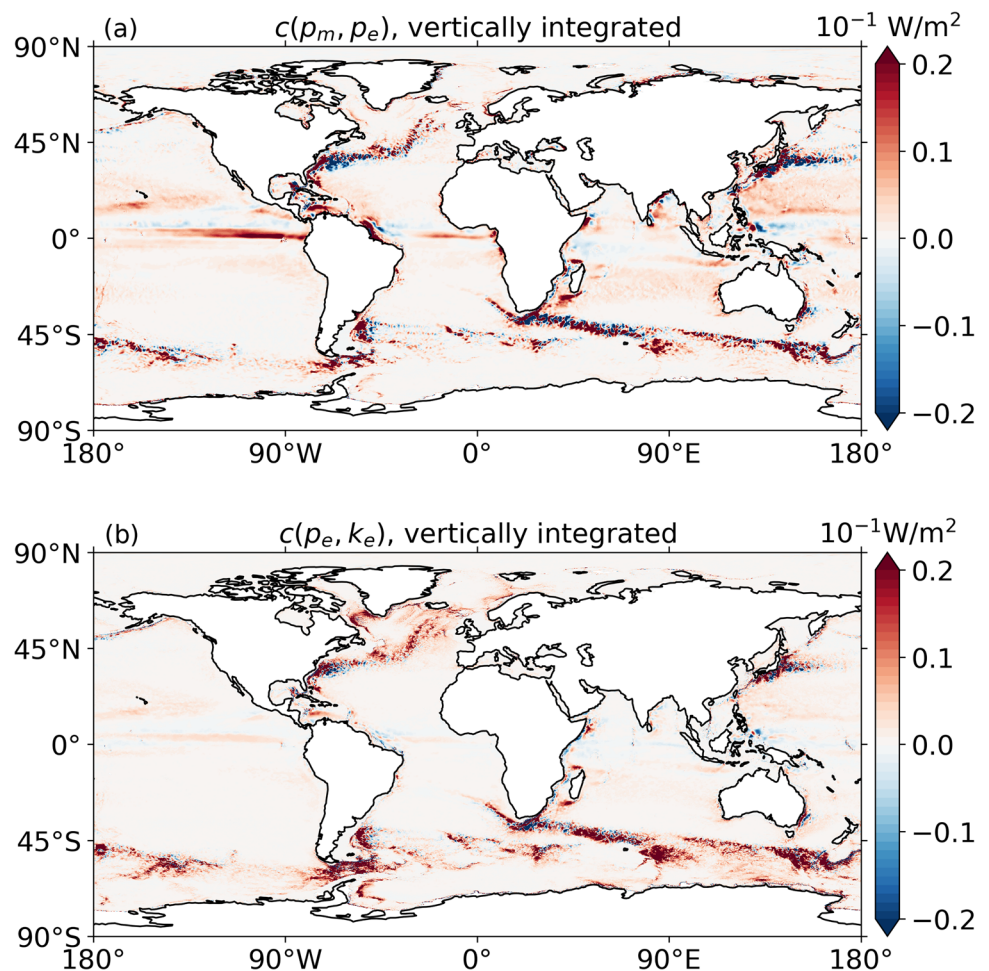
elsewhere. In the Southern Ocean, the baroclinic conversion, with magnitudes larger than 80 mW/m² , occurs up to a depth of 4 km. The strong conversion from p_m to p_e and to k_e found in the equatorial Pacific and equatorial Atlantic in Fig. 4 is confined to a thin surface layer.

Away from the baroclinic pathway, there is a sizable conversion of mean kinetic energy to mean available potential energy (i.e., negative $c(p_m, k_m)$). This happens where relatively dense water masses are moved upwards or relatively light water masses are moved downwards, resulting in the spatial distribution of $c(p_m, k_m)$ shown in Fig. 6 (top). Note that dense and light waters are defined relative to the reference density ρ_{ref}. The strong positive values along the equator result from upwelling of light water or more precisely upwelling of water lighter than ρ_{ref}. Generally, the distribution of $c(p_m, k_m)$ is strongly linked to the distribution of Ekman pumping/sucking velocity, which is predominantly strong in the upper 100 m in the equatorial region (Chereskin and Roemmich, 1991). Regions with strong Ekman velocities, e.g., the Southern Ocean, along eastern boundaries and the tropical ocean, have strong $c(p_m, k_m)$ conversion rates. The stronger negative values in the Southern Ocean are due

to upwelling of water denser than the reference density profile. In the mid-latitudes, the conversion is positive due to the down-welling of relatively dense water. The bottom panel of Fig. 6 shows that the conversion $c(p_m, k_m)$, with absolute magnitude of above 0.8 W/m², is confined to the upper 100 m near the equator, but extends to about 3000 m in the Southern Ocean. The horizontally integrated $c(p_m, k_m)$ is negative in the upper 3000 m and positive below (Fig. 7, left), indicating that the conversion is from the mean kinetic energy k_m to mean available potential energy p_m above but the other way around below 3000 m.

The weakest globally integrated conversion of the ICON/ NCEP LEC is that from mean kinetic energy to eddy kinetic energy (negative $c(k_e, k_m)$). Large values of $c(k_e, k_m)$ that change their sign within a short distance of a few grid cells are found in the Gulf Stream, Kuroshio, and in the frontal regions in the Southern Ocean (not shown). Loose et al. (2023) observed a similar behavior—abrupt sign change in the barotropic exchange term—after applying spatial filtering on simulations from an isopycnal 1/32° idealized model of the Southern and Atlantic ocean. When $c(k_e, k_m)$ integrated zonally (Fig. 8), a systematic picture emerges. We
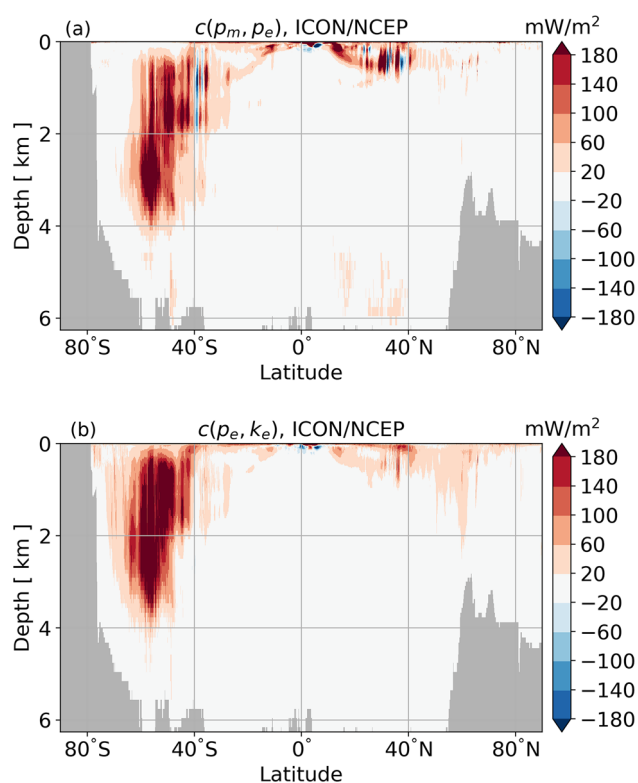
Fig. 5 Depth-latitude sections of the zonally integrated conversions $c(p_m, p_e)$ (top) and $c(p_e, k_e)$

find a conversion from mean kinetic energy to eddy kinetic energy (negative $c(k_e, k_m)$) in the upper 3 km of the ocean and a conversion from eddy kinetic energy to mean kinetic energy (positive $c(k_e, k_m)$) below 3 km. The former likely arises from barotropic instability due to the strong horizontal shears in the upper ocean velocities. The latter might be a sign of an inverse energy cascade where energy is transferred back from the eddy field (k_e) to the mean circulation (k_m). The vertical profile of horizontally integrated $c(k_e, k_m)$ (Fig. 7, right) confirms the reversal of the sign of $c(k_e, k_m)$ at about 2.8 km. It shows further that the strength of the conversion from k_m to k_e in the upper 100 to 200 m is much stronger than the opposite conversion from k_e to k_m with a maximum just below 4.5 km. Integrated not only horizontally but also vertically, this therefore results in a global energy conversion from k_m to k_e as the residue from counter acting energy fluxes.

4 Sensitivity of Lorenz energy cycle

In the following, we will discuss two sensitivities of the reference LEC obtained from ICON/NCEP: first with respect to the difference of LEC obtained with MPIOM/NCEP and second with respect to the difference LEC obtained

with ICON/ERA5. Fig. 3 shows the summary of the LEC derived from the ICON/NCEP (black), ICON/ERA5 (blue) and MPIOM/NCEP (red). Differences between the reference simulation — ICON/NCEP — and two other simulations — ICON/ERA5 and MPIOM/NCEP — are indicated by the numbers in brackets.

To estimate the significance of these changes, we compare them against the typical magnitude of LEC variability Δ arising from sampling errors. Therefore, we split the 10 years of the ICON/NCEP output into two 5-year chunks and estimate the LEC for each of these two chunks. This difference of the LEC components obtained from the two chunks of the same simulation is then Δ, our measure for the LEC variability due to sampling error that also exists without changing model or changing surface forcing (a more precise estimate of the sampling error is cost intensive and beyond the scope of this study). Hereafter, a model or forcing differences of single LEC components will be considered significant when they are larger than this Δ from sampling error variability. Only those differences which pass this "poor-man's" significance test are indicated in Fig. 3. In most cases, the model or forcing differences are, however, substantially larger than the sampling variability which gives us confidence that most observed changes can be considered as significant.

4.1 Sensitivity to model difference

The LEC terms derived from MPIOM/NCEP (red numbers in Fig. 3, taken from von Storch et al. (2012)) and those derived from ICON/NCEP (black numbers) reveal the following same gross features: First, the generation and dissipation terms balance each other to the lowest order and have magnitudes that are noticeably larger than those of the conversion terms. Secondly, the directions of all interior conversions are the same in MPIOM/NCEP and ICON/NCEP. Finally, the strongest pathway is the baroclinic pathway that converts P_m to P_e and eventually to K_e; the second strongest pathway is the conversion from mean kinetic energy K_m to mean available potential energy P_m; and the weakest one is the conversion from mean kinetic energy K_m to eddy kinetic energy K_e.

These agreements are encouraging, given that MPI-OM and ICON-O are two completely different ocean models since they suggest that the described gross features of the energy pathways are robust not only in terms of their directions, but also in terms of their magnitudes. For both models, the conversion from mean available potential energy P_m to eddy available potential energy P_e is about 0.8 TW, the conversion from mean kinetic energy K_m to eddy kinetic energy K_e is about $0.4 - 0.5$ TW, and the conversion from mean kinetic energy K_m to eddy kinetic energy K_e is about $0.1 - 0.2$ TW. While the similarity of these numbers is encour-

Fig. 6 (Top) horizontal distribution of the vertically integrated (above 100 m) conversion rate from mean available potential energy to mean kinetic energy, $c(p_m, k_m)$. (bottom) depth-latitude section of the zonally integrated $c(p_m, k_m)$
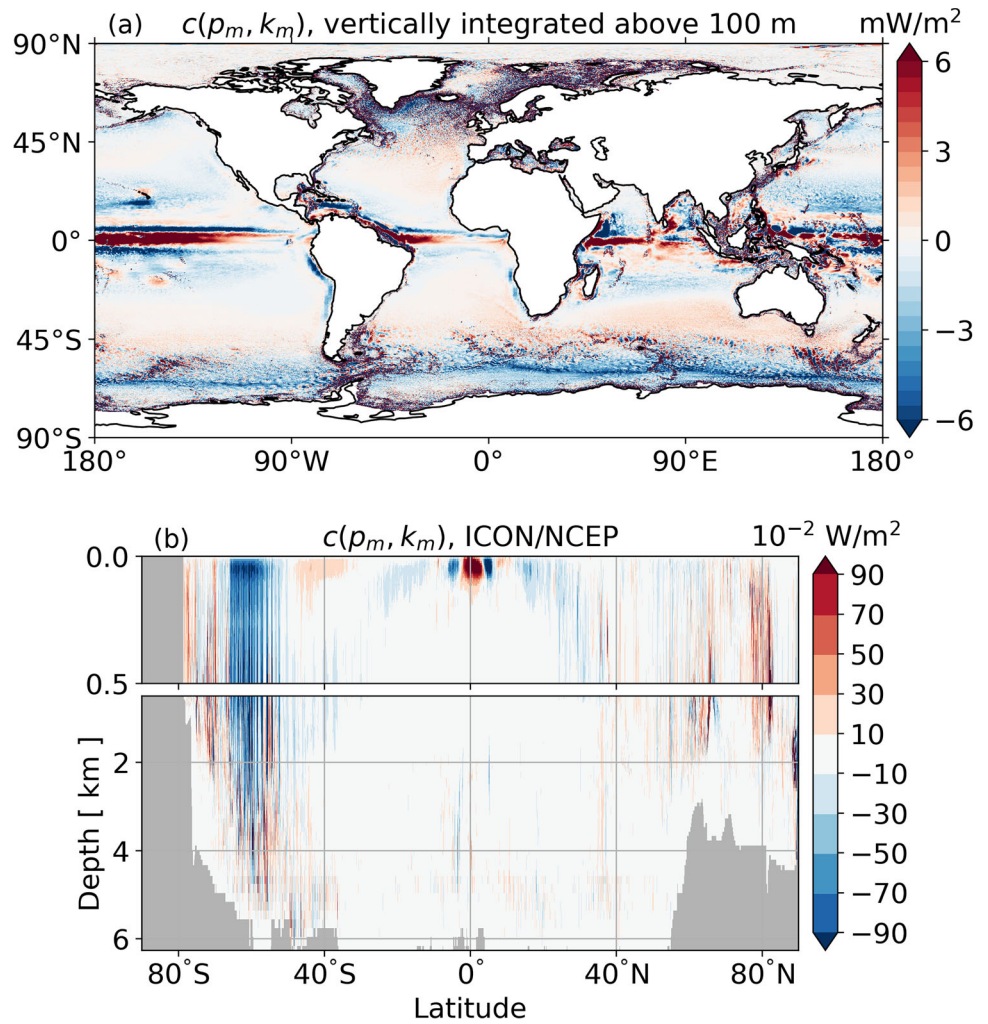
aging, it should also be noted that both models have relatively similar resolution over large parts of the ocean. Thus, both models do not resolve scales substantially smaller than the first baroclinic Rossby radius. To this end, they also do not resolve sub-mesoscale dynamics or lee wave generation by

eddies. We can therefore not conclude that the numbers which we obtain from the models considered here will also hold when these other dynamical regimes are explored.

Apart from the above common features, the LEC derived from ICON/NCEP, especially with respect to interior con-

Fig. 7 Vertical profiles of $c(p_m, k_m)$ (left) and $c(k_e, k_m)$
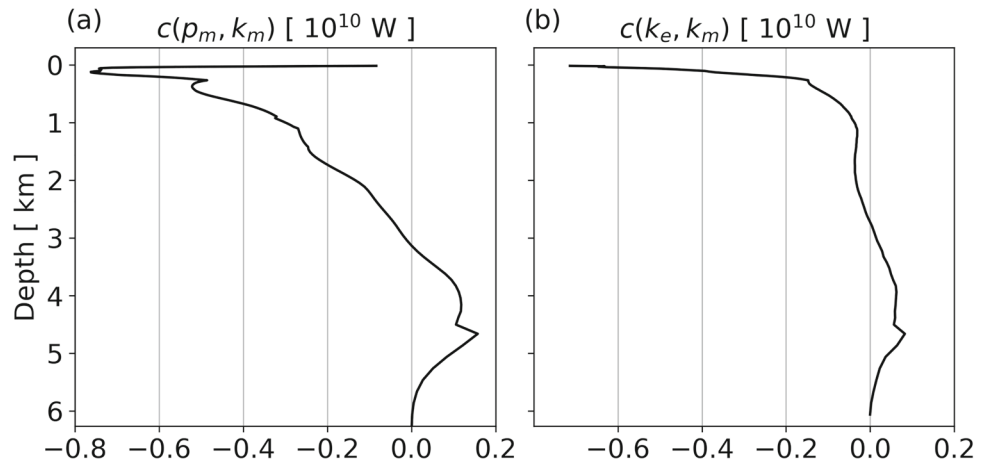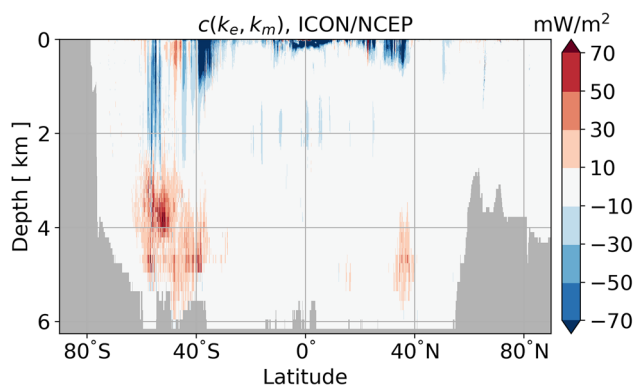
Fig. 8 Depth-latitude section of zonally integrated conversion $c(k_e, k_m)$

versions, deviates from that derived from MPIOM/NCEP in some aspects. While the first part of the baroclinic pathway, i.e., the conversion from P_m to P_e, is comparable in ICON/NCEP and MPIOM/NCEP, the second part of this pathway, i.e., from P_e to K_e, is about 50% stronger in MPIOM/NCEP than in ICON/NCEP. For the conversion from mean kinetic energy K_m to eddy kinetic energy K_e, it is about 30% stronger in ICON/NCEP than in MPIOM/NCEP. Below, we analyze these differences in the baroclinic pathway and in the barotropic pathway in more detail.

For the baroclinic pathway, we first compare the geographical distributions of vertically integrated $c(p_m, p_e)$ and $c(p_e, k_e)$ in ICON/NCEP (Fig. 4) with those in MPIOM/NCEP (Figs. 8 and 9 in von Storch et al. (2012)). These distributions compare well with each other, not only with respect to the locations of maxima of $c(p_m, p_e)$ and $c(p_e, k_e)$ in the regions of expected strong baroclinic instability along the Gulf Stream, Kuroshio, and the fronts in the Southern Ocean, but also in the central and eastern equatorial Pacific and the central and eastern equatorial Atlantic. Thus, the weaker conversion $C(P_e, P_m)$ in ICON/NCEP than in MPIOM/NCEP cannot be explained by the difference in the overall spatial distribution of these conversions.

Since the conversion $c(p_e, k_e)$ is determined by the covariance between density anomaly ρ' and vertical velocity anomaly w', we suspect that the weak conversion $C(p_e, k_e)$ in ICON/NCEP is related to the smaller magnitude of w' in ICON/NCEP than in MPIOM/NCEP. Given that the 3-dimensional velocity from MPIOM/NCEP is still available to us, we check this by calculating the standard deviation of w', $\sigma_{w'}$ and use the area averaged $\sigma_{w'}$ as a measure for typical magnitude of w' in ICON/NCEP and MPIOM/NCEP (Fig. 9, left). We find that in MPIOM/NCEP, $\sigma_{w'}$ is about factor 5 to 6 stronger between 50°S and 70°S than north of 10°N, reaching values of about 0.5 to 0.6 mm/s between 50°S and 70°S below 1 km (red solid and red dashed line). In ICON/NCEP, however, $\sigma_{w'}$ has comparable magnitude, around 0.1 to 0.2 mm/s, both between 50°S and 70°S and north of 10°N (black solid and black dash line). Some of these variations in w' may be correlated with ρ', resulting in weaker $C(P_e, P_m)$ in ICON/NCEP than in MPIOM/NCEP.

The large variability in w' shown in Fig. 9 can be, at least partially, related to quasi-geostrophic eddies emerging from baroclinic instability. Note that Fig. 10b points to a stronger eddy activity (stronger k_e) in the Southern Ocean in MPIOM/NCEP compared with ICON/NCEP. This stronger eddy activity in the Southern Ocean in MPIOM/NCEP is likely a consequence of the higher horizontal resolution of MPIOM/NCEP compared with ICON/NCEP.

From the assumption that the mesoscale eddy field is not causing substantial amounts of diapycnal mixing in the ocean interior, it would follow that $c(p_m, p_e)$ and $c(p_e, k_e)$ should have comparable magnitudes below the mixed layer. However, the numbers in Fig. 3 show that $C(P_e, K_e)$ is slightly weaker than $C(P_m, P_e)$ in MPIOM/NCEP. This highlights the effect of either upper ocean diapycnal mixing or non-physical numerical mixing.

In ICON/NCEP, this difference is even stronger, with $c(p_e, k_e)$ amounting to 58% of $c(p_m, p_e)$ in ICON/NCEP, compared to 88% in MPIOM/NCEP. The difference between the models suggests that the ICON-O configurations applied

Fig. 9 Standard deviation of w' over 5 years (2001–2005) (left) averaged horizontally over the latitudinal band from 70°S to 50°S (solid) and over the region north of 10°N (dashed), and the global averaged magnitude of the time-mean vertical velocity $|\overline{w}|$ (right) in MPIOM/NCEP (red) and in ICON/NCEP (black)
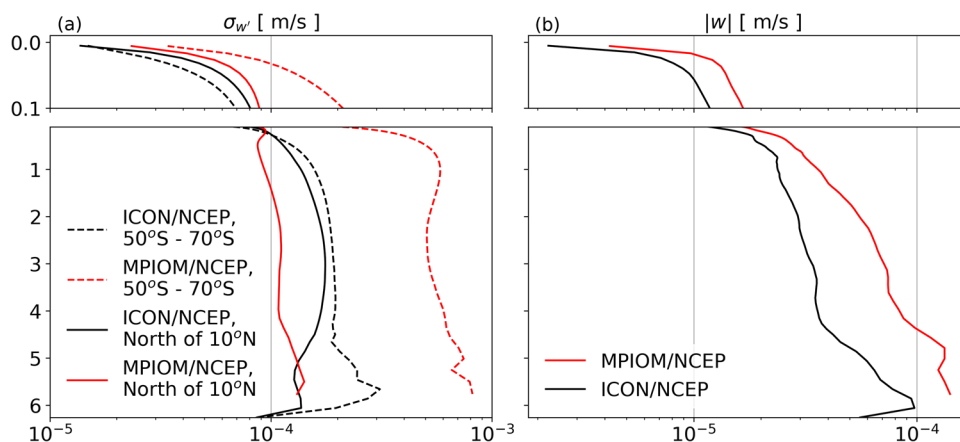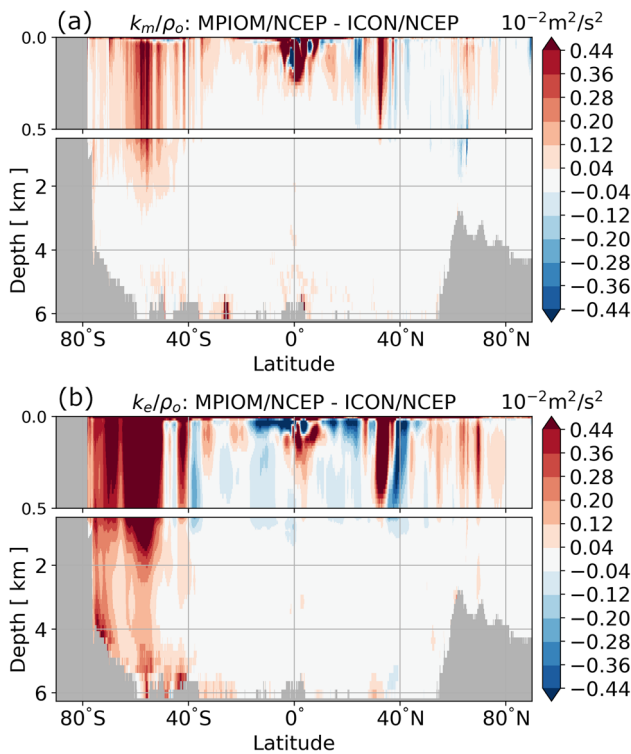
Fig. 10 Differences in zonally averaged $k_m/\rho_\circ$ between MPIOM/NCEP and ICON/NCEP (top) and in zonally averaged $k_e/\rho_\circ$ between MPIOM/NCEP and ICON/NCEP (bottom) in m^2/s^2

here have more diapycnal mixing compared to MPIOM. Support for this hypothesis comes from the result of Mohammadi-Aragh et al. (2015) that in a configuration with a lower grid Reynolds number, baroclinic instability occurring close to the grid scale can lead to higher numerical mixing. With the lower resolution of ICON-O than in MPI-OM in the eddy-active Southern Ocean, the grid Reynolds number in ICON-O is lower than that in MPI-OM there. The numerical dissipation of p_e and k_e and with that the reduction in $c(p_e, k_e)$ can be stronger in the Southern Ocean in ICON-O than in MPI-OM.

Probably, the strength of $C(P_e, K_e)$ in ICON/NCEP can be enhanced by increasing the resolution at higher latitudes; however, this investigation is beyond the scope of this study. It remains an open question to which degree the diapycnal mixing responsible for the dissipation of p_e in all model simulations (but strongest in ICON) is caused by diabatic processes in the upper-ocean mixed layer or by interior physical or numerical water mass conversions.

For the barotropic pathway described by $c(k_m, k_e)$, whose global integral is smaller in MPIOM/NCEP (0.11 TW) than in ICON/NCEP (0.17 TW), we compare the vertical profile of horizontal integrated $c(k_e, k_m)$ shown in Fig. 7 (right) with the same profile derived from MPIOM/NCEP (Fig.11a) in von Storch et al. (2012). Both profiles show a similar sign reversal around 2.5 to 3 km. However, the horizontal inte-

gral of $c(k_e, k_m)$ is noticeably smaller in the ocean interior in ICON/NCEP than in MPIOM/NCEP. The maximum of the positive conversion from k_e to k_m around 4 km amounts to about 0.35×10^{10} W in MPIOM/NCEP but is below 0.1×10^{10} W in ICON/NCEP. So the larger value of $C(K_m, K_e)$ in ICON/NCEP is caused by weaker counter conversion in the deep ocean in ICON/NCEP than in MPIOM/NCEP.

For the conversion from mean kinetic energy to mean available potential energy $c(k_m, p_m)$, whose global value is larger in MPIOM/NCEP than in ICON/NCEP, we compare the vertical profile of horizontally integrated $c(p_m, k_m)$ shown in Fig. 7 (left) with the same profile derived from MPIOM/NCEP (Fig.12 in von Storch et al. (2012)). Both profiles show negative values of $c(p_m, k_m)$ above 3 km and positive values below 3 km. However, the magnitude of $c(p_m, k_m)$ is larger in MPIOM/NCEP than that in ICON/NCEP. The minimum of the horizontally integrated $c(p_m, k_m)$ amounts almost to -1.5×10^{10} W in MPIOM/NCEP, but is barely -0.8×10^{10} W in ICON/NCEP. The maximum of the horizontally integrated $c(p_m, k_m)$ at about 4 km amounts to about 0.6×10^{10} W in MPIOM/NCEP, but reaches barely 0.2×10^{10} W in ICON/NCEP. The smaller magnitude of $c(p_m, k_m)$ in ICON/NCEP compared with MPIOM/NCEP is most likely caused by a weaker time-mean vertical velocity in ICON/NCEP than in MPIOM/NCEP as can be inferred from Fig. 9b. Since the same surface forcing is used, the increase in mean vertical velocity is likely caused by the different time-mean circulations in ICON/NCEP and MPIOM/NCEP. When integrated globally, the strong conversion from K_m to P_m in MPIOM/NCEP results in a global $C(K_m, P_m)$ of about 0.49 TW, which is larger than $C(K_m, P_m)$ of about 0.4 TW in ICON/NCEP.

4.2 Sensitivity to forcing difference

In this section, we assess the sensitivity of the global LEC to surface forcing by comparing the LEC terms derived from ICON/ERA5 (blue numbers in Fig. 3) with those derived from ICON/NCEP (black numbers).

For each of the four energy compartments, K_m, K_e, P_m, and P_e, the generation terms increase substantially. However, also the dissipation terms increase by nearly the same amount (compare blue bracketed numbers in Fig. 3 for the forcing differences in the generation and dissipation terms). More specifically, $G(K_e)$ is increased by about 42% from its value in ICON/NCEP and becomes almost 1 TW stronger in ICON/ERA5. The generation of eddy available potential energy $G(P_e)$ is increased by about 23% from its value in ICON/NCEP and becomes almost 0.2 TW stronger in ICON/ERA5.

Figure 13 shows that the large increases in the generation of eddy kinetic energy $g(k_e)$ are most dominant in the mid- to high-latitude regions, whereas the large increases in the gen-

eration of eddy available potential energy $g(p_e)$ are more concentrated on the Gulf Stream and Kuroshio region. Dissipation increases in ICON/ERA5 by about 36% for K_e and 18% for P_e. Regarding the mean kinetic energy and mean available potential energy, the increases in the generation, reaching 13% in $G(K_m)$ and 15% in $G(P_m)$, are accompanied by increases in dissipation as well, reaching 16% in K_m and 15% in P_m.

The largest changes in the conversion terms concern the barotropic pathway from K_m to K_e, which is about 24%, or 0.04 TW, stronger in ICON/ERA5 than in ICON/NCEP. The baroclinic pathway increases by about 8% for $C(P_m, P_e)$ and 6% for $C(P_e, K_e)$ in ICON/ERA5 than in ICON/NCEP. The conversion from K_m to P_m is not notably affected by the forcing difference. Except for $C(K_m, P_m)$, forcing-induced changes in all terms of the LEC are statistically significant with respect to our "poor man's" test. Nevertheless, since the test is not precise, we will focus only on the biggest change in the generation $G(K_e)$ and the biggest relative change in the conversion $C(K_m, K_e)$. Both affect the eddy kinetic energy K_e.

We start our consideration with the forcing difference in conversion $c(k_e, k_m)$. Figure 11 shows that the mean kinetic energy k_m is more strongly converted to eddy kinetic energy in ICON-ERA5 than in ICON/NCEP in the upper 500 m in the low-latitude oceans equator-ward of about 40°. This latitudinal band coincides roughly with the band where the time-mean wind stress is stronger in ERA5 than in NCEP (upper right panel in Fig. 2). Integrated globally, the generation of mean kinetic energy is somewhat stronger in ICON/ERA5 than in ICON/NCEP. We hence hypothesize that the stronger mean wind stress in ERA5 leads to a stronger generation in mean kinetic energy and with that stronger time-mean currents. Figure 12a shows indeed that apart from a few interruptions by narrow latitudinal bands where k_m decreases, the zonally averaged value in ICON/ERA5 is increased from 40°S to 45°N; albeit, the
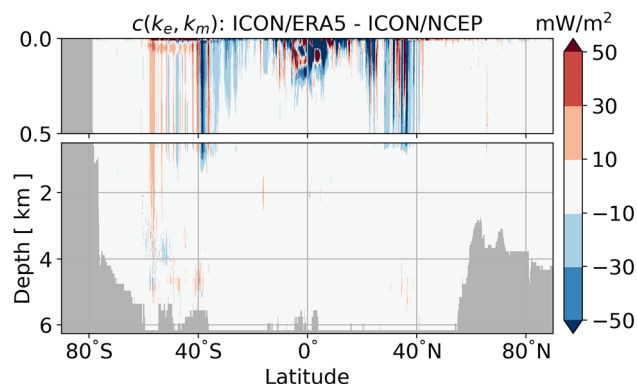
Fig. 11 Differences in the conversion $c(k_e, k_m)$ between ICON/ERA5 and ICON/NCEP
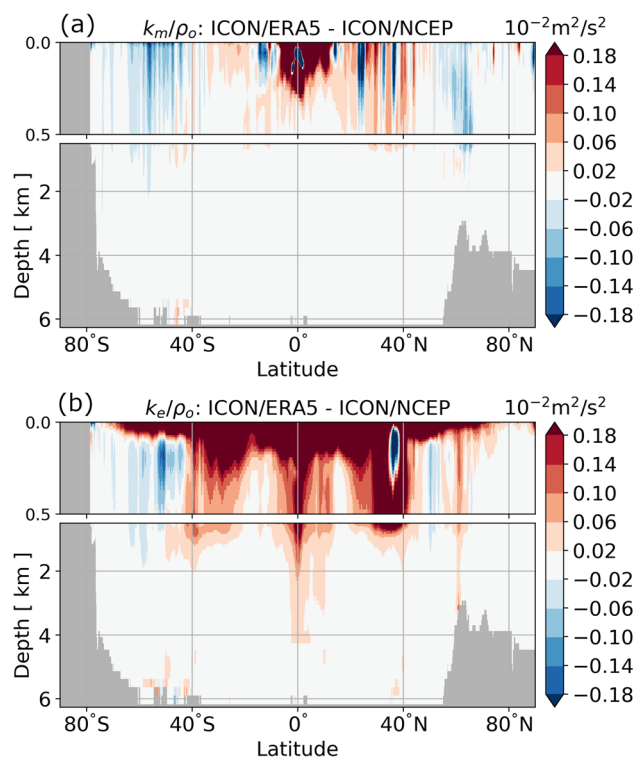
Fig. 12 Differences in zonally averaged k_m/ρ_o between ICON/ERA5 and ICON/NCEP (top) and in zonally averaged k_e/ρ_o between ICON/ERA5 and ICON/NCEP (bottom) in m^2/s^2

increase is much stronger in the tropical oceans from about 10°S to 10°N. The stronger time-mean currents could then lead to a stronger conversion $c(k_m, k_e)$. The enhanced zonally averaged k_e equator-ward of about 40° above roughly about 500 m (Fig. 12b) could be the result of the stronger conversion $c(k_m, k_e)$ in ICON/ERA5 than in ICON/NCEP.

We consider now the largest forcing difference found in the generation of eddy kinetic energy $g(k_e)$, which amounts to nearly 1 TW when integrated globally. Figure 13 shows that $g(k_e)$ is almost everywhere stronger in ICON/ERA5 than in ICON/NCEP. The stronger generation is due to the stronger wind stress variability in ERA5 than in NCEP (Fig. 1). It is however unclear how the higher variability in surface winds should systematically generate an enhanced eddy field (note that this requires a correlation between the wind fluctuations which typically occur on time scales of hours to days and the eddy field which acts on time scales of weeks to months). The more likely explanation is that the stronger wind fluctuations in ERA5 lead to an enhanced excitation of ageostrophic dynamics like inertial oscillations. Such enhanced excitation in ICON/ERA5 relative to ICON/NCEP is consistent with the systematic increase in the generation of near-inertial motions with increasing temporal resolution of the wind forcing found by Rimac et al. (2013).

According to Rimac et al. (2016), most of the excited inertial oscillations (about 90%) dissipate within the ocean's

Fig. 13 Differences in eddy kinetic energy generation g_{k_e} (top) and in eddy available potential energy generation $g(p_e)$ (bottom) between ICON/ERA5 and ICON/NCEP
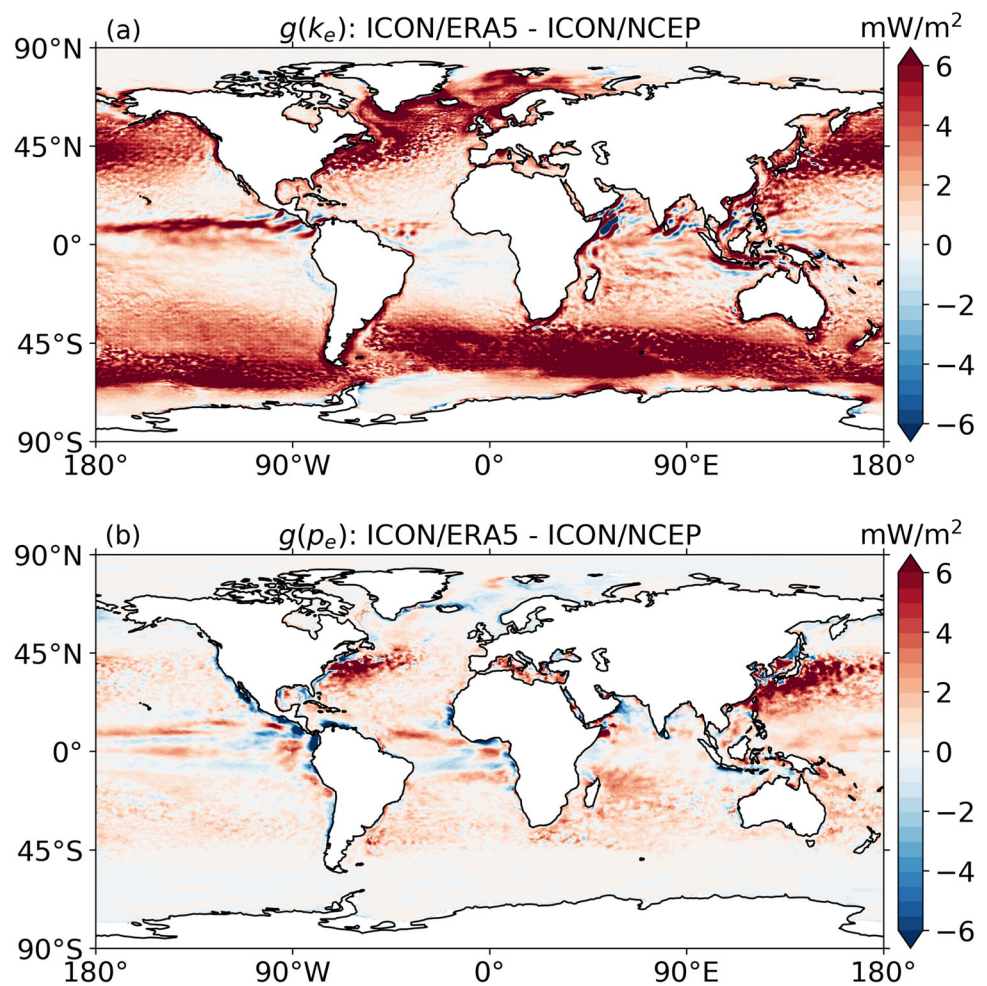
mixed layer. This could affect the fate of the nearly 1 TW stronger generation $G(K_e)$ due to the wind stress fluctuations in ERA5.

It will be interesting to see from future studies with higher resolution model configurations (e.g., resolving submesoscale dynamics) and more energetically consistent parameterizations (e.g., allowing additional energy fluxes from k_e to either a parameterized internal wave or turbulent kinetic energy compartment) whether and how a feedback between the k_e compartment and the resolved circulation is established.

5 Summary

In this paper, we investigate the sensitivity of the LEC to model difference and to forcing difference. The investigation due to model difference is based on two pairs of ocean-only simulations at nominal O(10 km) resolution. The first pair consists of ICON/NCEP and MPIOM/NCEP, performed with two ocean general circulation models with completely different model architectures—MPI-OM and ICON-O—driven

by the same surface forcing (NCEP). The second investigation due to forcing difference is based on the ICON/NCEP and ICON/ERA5 simulations, performed both with the same ocean model and configuration (namely, ICON-O with 10 km resolution) but driven by surface fluxes obtained from two different reanalyses—NCEP and ERA5.

The first remarkable result which we obtain is the relative insensitivity of the energy conversions between the different compartments of the LEC—no matter whether we consider a forcing or a model difference. In particular, we note that not only the directions of the conversions stay the same but also the magnitudes of the LEC terms themselves as well as the overall spatial distributions of the conversion terms change little, no matter whether we consider the forcing or the model differences.

Despite these overall similarities, we also detect differences when comparing the underlying ICON-O to MPI-OM simulations. The first one concerns the baroclinic pathway that converts mean available potential energy p_m to eddy available potential energy p_e via $c(p_m, p_e)$ and further converts eddy available potential p_e to eddy kinetic energy k_e via $c(p_e, k_e)$. We find that the first transformation $c(p_m, p_e)$

is comparable in both simulations but the second $c(p_e, k_e)$ is considerably weaker in ICON. Consequently, there is enhanced dissipation of p_e in ICON/NCEP compared with MPIOM/NCEP. This might be related to the coarser resolution of the ICON-O configuration in the Southern Ocean where the resolution of 10 km only marginally resolves the first baroclinic Rossby radius. This probably leads to a too strong damping of the eddy kinetic energy field and to too strong diabatic mixing which reduces the eddy available potential energy.

The second difference concerns the conversion $c(k_m, k_e)$ in the deep ocean, which is in the opposite direction compared to the upper 2.5 km. This deep conversion, which is noticeably weaker and results in a larger global value of $C(K_m, K_e)$ in ICON/NCEP than in MPIOM/NCEP, is likely related to the weaker mesoscale eddies in ICON/NCEP which also most likely reduces the amount of energy transferred towards larger scales and therewith the mean circulation in the case of geostrophic turbulence.

The third difference concerns the conversion $c(p_m, k_m)$, which quantifies the generation of mean available potential energy in terms of wind-driven Ekman velocity. The $c(p_m, k_m)$ term is weaker in ICON/NCEP than in MPIOM/ NCEP, due to weaker mean vertical velocity in ICON/NCEP than in MPIOM/NCEP.

The largest change among the terms of the LEC induced by forcing difference when comparing ICON/NCEP with ICON/ERA5 is the increase in the generation of eddy kinetic energy $g(k_e)$. Integrated globally, $G(K_e)$ is larger than all other generation terms. Using high-frequency ERA5 wind stress further increases $G(K_e)$ obtained from NCEP wind stress by about 1 TW. This enhanced generation is most likely balanced by an enhanced dissipation of eddy kinetic energy in the ocean's mixed layer, without having strong effects on the interior circulation. Note that in addition to the mesoscale eddy field, transient motions such as inertial oscillations are part of what we refer to as eddy dynamics (e.g., k_e but also $D(k_e)$).

The gross features of the LEC pictures the ocean as a "windmill" which transfers the forcing of the ocean by the winds into the circulation of the ocean (von Storch et al., 2012). The insensitivity of the LEC with respect to the enhanced high-frequent wind forcing ($G(k_e)$) indicates that this "windmill" is not able to effectively use this enhanced energy input for large scale currents. In this regard, it might be considered as an inefficient "windmill" regarding the large-scale circulation. On the other hand, it may become a more efficient "mixer" since the energy within the inertial oscillations and internal waves might ultimately lead to energy transfers from these compartments to small-scale turbulence. In parts, this is already reflected by the TKE scheme used in our ICON configurations where energy dissipated by

vertical shear is transferred to turbulent kinetic energy. It will be interesting to observe to what degree such energy pathways change if simulations are performed at higher resolutions, such as those in which sub-mesoscale dynamics and a larger fraction of the internal wave field are resolved. Changes in the LEC may also be expected when more sophisticated parameterizations are used, such as those which enable consistent transfers between resolved and unresolved energy compartments.

Appendix Terms of the LEC

Here, we limit ourselves to presenting the terms of the LEC. The derivation is presented in the appendix of von Storch et al. (2012). The symbols used in the equations below are defined in Table 2. Mean available potential energy, P_m

$$P_m = \int_V p_m \mathrm{d}V, \quad p_m = -\frac{1}{2}\frac{g}{n_\circ}\overline{\rho^*}^2 \tag{A1}$$

Mean kinetic energy, K_m

$$K_m = \int_V k_m \mathrm{d}V, \qquad k_m = \frac{1}{2}\rho_\circ(\overline{u}^2 + \overline{v}^2) \tag{A2}$$

Eddy available potential energy, P_e

$$P_e = \int_V p_e \mathrm{d}V, \qquad p_e = -\frac{1}{2}\frac{g}{n_\circ}\overline{\rho'^2} \tag{A3}$$

Eddy kinetic energy, K_e

$$K_e = \int_V k_e \mathrm{d}V, \qquad k_e = \int_V \frac{1}{2}\rho_\circ\overline{(u'^2 + v'^2)}\mathrm{d}V \tag{A4}$$

In a steady state, P_m, P_e, K_m, and K_e satisfy,

$$\frac{\mathrm{d}P_m}{\mathrm{d}t} = C(P_e, P_m) - C(P_m, K_m) + G(P_m) - D(P_m) = 0 \tag{A5}$$

$$\frac{\mathrm{d}P_e}{\mathrm{d}t} = -C(P_e, P_m) - C(P_e, K_e) + G(P_e) - D(P_e) = 0 \tag{A6}$$

$$\frac{\mathrm{d}K_m}{\mathrm{d}t} = C(K_e, K_m) + C(P_m, K_m) + G(K_m) - D(K_m) = 0 \tag{A7}$$

$$\frac{\mathrm{d}K_e}{\mathrm{d}t} = -C(K_e, K_m) + C(P_e, K_e) + G(K_e) - D(K_e) = 0 \tag{A8}$$

where

$$G(P_m) = \int_S g(p_m)\mathrm{d}S, \qquad g(p_m) = -g\frac{\alpha_{\circ,1}}{n_\circ}\overline{J_s\rho^*} - g\frac{\beta_{\circ,1}}{n_\circ}\overline{G_s\rho^*} \tag{A9}$$

Table 2 List of symbols

g	Acceleration due to gravity
ρ	Density
ρ_{ref}	Reference density. Area average of the time-mean density
	Constant at a given model level
ρ^*	Density anomaly, $\rho^* = \rho - \rho_{ref}$
$\rho_\circ$	1025.022 kg m^{-3}
$n_\circ$	Vertical gradient of the time mean local potential density
$\mathbf{u}\ (u, v, w)$	3D velocity
$\mathbf{u_h}\ (u, v)$	Horizontal velocity
$'$ (prime)	Variation in time
$^-$ (overbar)	Time mean
D	Energy dissipation. Derived as residual from the respective balance equation
G	Energy generation
C	Energy conversion. From X to Y, C(X,Y). From Y to X, C(Y,X) $\equiv$ -C(X,Y)
$\alpha_{\circ,1}$	Thermal expansion coefficient in uppermost model layer
$\beta_{\circ,1}$	Haline contraction coefficient in uppermost model layer
J_s	Temperature flux. $J_s = (\frac{1}{\rho_s C})H$ where H is the total heat flux at the sea surface
	$C = 4000$ J(Kg K)$^{-1}$ is the specific heat capacity of seawater, and ρ_s is the density
	at the sea surface
G_s	Salinity flux. $G_s = \overline{S_1}(E - P)$, where E is the evaporation rate and P the precipitation
	rate at the sea surface and S_1 the time-mean salinity in the uppermost model layer
$\tau\ (\tau_{x,s}, \tau_{y,s})$	Stress exerted by the atmosphere on the ocean

$$G(P_e) = \int_S g(p_e)\mathrm{d}S, \qquad g(p_e) = -g\frac{\alpha_{\circ,1}}{n_\circ}\overline{\rho' J_s'} - g\frac{\beta_{\circ,1}}{n_\circ}\overline{\rho' G_s'} \quad (A10)$$

$$G(K_m) = \int_S g(k_m)\mathrm{d}S, \qquad g(k_m) = \overline{\tau_{x,s}}\ \overline{u} + \overline{\tau_{y,s}}\ \overline{v} \quad (A11)$$

$$G(K_e) = \int_S g(k_e)\mathrm{d}S, \qquad g(k_e) = \overline{\tau_{x,s}' u'} + \overline{\tau_{y,s}' v'} \quad (A12)$$

$$C(P_e, P_m) = \int_V c(p_e, p_m)\mathrm{d}v, \qquad c(p_e, p_m) = -\frac{g}{n_\circ}\overline{\rho' \mathbf{u_h'}} \cdot \nabla_h \overline{\rho} \quad (A13)$$

$$C(K_e, K_m) = \int_V c(k_e, k_m)\mathrm{d}v, \qquad c(k_e, k_m) = \rho_\circ(\overline{u'\mathbf{u'}}\cdot\nabla\overline{u} + \overline{v'\mathbf{u'}}\cdot\nabla\overline{v}) \quad (A14)$$

$$C(P_m, K_m) = \int_V c(p_m, k_m)\mathrm{d}v, \qquad c(p_m, k_m) = -g\overline{\rho^*}\ \overline{w} \quad (A15)$$

$$C(P_e, K_e) = \int_V c(p_e, k_e)\mathrm{d}v, \qquad c(p_e, k_e) = -g\overline{\rho' w'} \quad (A16)$$

Declarations

References

Bishop SP, Small RJ, Bryan FO (2020) The global sink of available potential energy by mesoscale air-sea interaction. Journal of Advances in Modeling Earth Systems 12(10):2020–002118

Chereskin T, Roemmich D (1991) A comparison of measured and wind-derived Ekman transport at 11 N in the Atlantic Ocean. J Phys Oceanogr 21(6):869–878

Gaspar P, Grégoris Y, Lefevre J-M (1990) A simple eddy kinetic energy model for simulations of the oceanic vertical mixing: tests at station Papa and long-term upper ocean study site. Journal of Geophysical Research: Oceans 95(C9):16179–16193. https://doi.org/10.1029/JC095iC09p16179

Gent PR, Mcwilliams JC (1990) Isopycnal mixing in ocean circulation models. J Phys Oceanogr 20(1):150–155

Hersbach H, Bell B, Berrisford P, Hirahara S, Horányi A, Muñoz-Sabater J, Nicolas J, Peubey C, Radu R, Schepers D, Simmons A, Soci C, Abdalla S, Abellan X, Balsamo G, Bechtold P, Biavati G, Bidlot J, Bonavita M, De Chiara G, Dahlgren P, Dee D, Diamantakis M, Dragani R, Flemming J, Forbes R, Fuentes M, Geer A, Haimberger L, Healy S, Hogan RJ, Hólm E, Janisková, M, Keeley, S, Laloyaux, P, Lopez, P, Lupu, C, Radnoti, G, Rosnay, P, Rozum, I, Vamborg, F, Villaume, S, Thépaut, J-N, (2020) The ERA5 global reanalysis. Q J R Meteorol Soc 146(730):1999–2049

Jungclaus, JH, Fischer, N, Haak, H, Lohmann, K, Marotzke, J, Matei, D, Miko-lajewicz, U, Notz, D, Storch, JS (2013) Characteristics of the ocean simula- tions in the Max Planck Institute Ocean Model (MPIOM) the ocean component of the MPI-Earth system model. J. Adv. Model. Earth Syst. **5**:422–446. https://doi.org/10.1002/jame.20023

Kalnay E, Kanamitsu M, Kistler R, Collins W, Deaven D, Gandin L, Iredell M, Saha S, White G, Woollen J, Zhu Y, Chelliah M, Ebisuzaki W, Higgins W, Janowiak J, Mo KC, Ropelewski C, Wang J, Leetmaa A, Reynolds R, Jenne R, Joseph D (1996) The NCEP/NCAR 40-year reanalysis project. Bulletin of the American Meteorological Society 77(3):437–472

Kim Y, Kim M (2013) Examination of the global lorenz energy cycle using MERRA and NCEP-reanalysis 2. Clim Dyn 40:1499–1513

Korn P (2017) Formulation of an unstructured grid model for global ocean dynamics. J Comput Phys 339:525–552

Korn P, Brüggemann N, Jungclaus JH, Lorenz SJ, Gutjahr O, Haak H, Linardakis L, Mehlmann C, Mikolajewicz U, Notz D, Putrasahan DA, Singh V, Storch J-S, Zhu X, Marotzke J (2022) ICON-O: the ocean component of the ICON Earth system model-global simulation characteristics and local telescoping capability. Journal of Advances in Modeling Earth Systems 14(10):2021–002952

Li L, Ingersoll AP, Jiang X, Feldman D, Yung YL (2007) Lorenz energy cycle of the global atmosphere based on reanalysis datasets. Geophys Res Lett 34(16)

Loose N, Bachman S, Grooms I, Jansen M (2023) Diagnosing scale-dependent energy cycles in a high-resolution isopycnal ocean model. J Phys Oceanogr 53(1):157–176

Lorenz, EN (1967) The nature and theory of the general circulation of the atmosphere. WMO- No. 218, pp 161. WMO

Lorenz EN (1955) Available potential energy and the maintenance of the general circulation. Tellus 7:157–167

Marques C, Rocha A, Corte-Real J, Castanheira J, Ferreira J, Melo-Goncalves P (2009) Global atmospheric energetics from NCEP-reanalysis 2 and ECMWF-ERA40 reanalysis. Int J Climatol 29:159–174

Marsland SJ, Haak H, Jungclaus JH, Latif M, Röske F (2003) The Max-Planck-institute global ocean/sea ice model with orthogonal curvilinear coordinates. Ocean Model 5(2):91–127

Mohammadi-Aragh M, Klingbeil K, Brüggemann N, Eden C, Burchard H (2015) The impact of advection schemes on restratifiction due to lateral shear and baroclinic instabilities. Ocean Model 94:112–127

Oort A (1964) On estimates of the atmospheric energy cycle. Mon Weather Rev 11:483–493

Oort AH, Anderson LA, Peixoto JP (1994) Estimates of the energy cycle of the oceans. Journal of Geophysical Research: Oceans 99(C4):7665–7688

Pacanowski RC, Philander SGH (1981) Parameterization of vertical mixing in numerical models of tropical oceans. J Phys Oceanogr 11:1443–1451

Rimac A, Storch J-S, Eden C, Haak H (2013) The influence of high-resolution wind stress field on the power input to near-inertial motions in the ocean. Geophys Res Lett 40(18):4882–4886

Rimac A, Storch JS, Eden C (2016) The total energy flux leaving the ocean's mixed layer. J Phys Oceanogr 46:1885–1900

Röske F (2006) A global heat and freshwater forcing dataset for ocean models. Ocean Model 11(3–4):235–297

Storch J-S (2019) Energetics of the climate system. Oxford Research Encyclopedias. https://doi.org/10.1093/acrefore/9780190228620.013.88

Storch J-S, Eden C, Fast I, Haak H, Hernández-Deckers D, Maier-Reimer E, Marotzke J, Stammer D (2012) An estimate of the Lorenz energy cycle for the world ocean based on the STORM/NCEP simulation. J Phys Oceanogr 42(12):2185–2205

Winters KB, Lombard PN, Riley JJ, D'Asaro EA (1995) Available potential energy and mixing in densitystratified fluids. J Fluid Mech 289:115–228

Zhai X, Johnson HL, Marshall DP, Wunsch C (2012) On the wind power input to the ocean general circulation. J Phys Oceanogr 42(8):1357–1365